Appl. Phys. B 75, 779–790 (2002)
DOI: 10.1007/s00340-002-1038-x

Applied Physics B
Lasers and Optics

J. LUQUE*
R.J.H. KLEIN-DOUWEL**
J.B. JEFFRIES***
G.P. SMITH✉
D.R. CROSLEY

Quantitative laser-induced fluorescence of CH in atmospheric pressure flames

Molecular Physics Laboratory, SRI International, 333 Ravenswood Avenue, Menlo Park, California 94025, USA

Received: 27 March 2002/Revised version: 22 August 2002
Published online: 15 November 2002 • © Springer-Verlag 2002

ABSTRACT Absolute number densities of the CH radical were determined in a partially premixed methane/air flame (equivalence ratio was 1.36) at atmospheric pressure by exciting a predissociating level via the CH B–X(1,0) transition using a quasi-linear laser-induced fluorescence scheme. The peak number density was $(1.0 \pm 0.4) \times 10^{13}$ cm^{-3} or 2.4 ± 1 ppm at 1900 K, with a flame-front width of 250 μm (FWHM). Rotational energy transfer must be considered for correct laser-induced fluorescence signal interpretation. Competition between optical pumping and rotational relaxation in both excited and ground states produces a signal that varies almost linearly with laser pulse energy even for large pumping rates. For these conditions, the population of the initial ground-state rotational level is depleted by optical pumping, and rotational energy transfer collisions rapidly repopulate the level during the laser pulse. Deviations from linear behavior are less than 20%. The effects of spatial resolution and polarization of the fluorescence on the absolute measurements are also discussed.

PACS 82.80.Dx; 42.62-b; 34.50.Ez

1 Introduction

Determination of absolute concentrations of intermediate species is an important and active goal of combustion diagnostics [1–17]. The need to test kinetic and fluid dynamic models drives laser spectroscopic diagnostics research to provide fully quantitative results. Only a few years ago, relative concentration measurements and spatial distribution gradients of intermediate species in diffusion and premixed flames were sufficient to test combustion model predictions. However, recent progress in temperature- and pressure-dependent chemical mechanisms and the computational power to include finite-rate chemistry and fluid transport provides combustion model predictions that require quantitative concentration measurements for adequate tests.

Laser-induced fluorescence (LIF) and absorption spectroscopies are common experimental methods for measuring trace species in combustion [18]. Absorption methods are being revitalized by new techniques like cavity ring-down spectroscopy (CRD) [19, 20] and frequency-modulated spectroscopy (FM) [21], which are much more sensitive than traditional absorption techniques and compete with LIF in situations where spatial information is not important. LIF is the technique more widely used to measure radicals in flames because of its spatial resolution, high-sensitivity chemical species selectivity and relative ease of interpretation. However, LIF also presents technical difficulties, such as non-universality, dependence on ground- and excited-state collisional dynamics and non-trivial extraction of absolute number densities.

The main challenges to obtaining reliable quantitative LIF measurements are calibration of the optical detection system, fluorescence quantum yield determination and assessment of the competition between optical pumping, collisional redistribution and excited-state deactivation. Only in very specific situations can these problems be avoided, for example as Versluis *et al.* [17] have shown using a OH A–X(0,0) bi-directional planar LIF approach in a highly absorptive flame. They obtained OH absolute number densities without any external calibration and quenching knowledge. For other systems, calibration issues can be solved by:

a) simultaneously measuring LIF signals from the same molecule at known concentrations; NO [22], CO [10], HCO [7] and CH_2O [23] are typical examples;

b) comparing the LIF with that from a different molecule with similar spectroscopic properties and known concentration: CF calibrated with NO [24], CH calibrated with N_2^+ [25]. A significant advantage of calibration with the LIF signal is the ability to account for saturation and collisional effects;

c) using other optical techniques like Raman and Rayleigh scattering to determine the experimental optical collection factor. For example: CH, C_2 and CN [1, 2, 4, 26–31];

d) measuring the column density by absorption and combining it with the path length to normalize the LIF signal; OH is the radical most commonly calibrated in this way [10, 22]. As sensitive absorption techniques become available, the

✉ Fax: +1-650/859-6196, E-mail: smith@mplvax.sri.com
*Present address: Lam Research Corporation, Fremont, CA 94538, USA
**Present address: Mechanical Engineering, Eindhoven University of Technology, 5600 MB Eindhoven, The Netherlands
***Present address: Mechanical Engineering Dept., Stanford University, Stanford CA 94305, USA

combination of LIF spatial profiles normalized by CRD is more common [11, 12, 32, 33].

The first attempts to measure absolute radical concentrations using LIF relied on saturated excitation techniques (strong-field approximation) [26, 34]. In this high laser power regime, the population promoted to the upper state is independent of collisional quenching and laser power, and this promises a simple interpretation of the fluorescence signal and a superior signal-to-noise ratio. However, this approach experiences problems related to incomplete spatial, temporal and spectral saturation, leading to apparent concentrations larger than those measured by absorption methods [26]. More refined saturation models offer better agreement [30, 35, 36], but the signal interpretation is not simple. A second approach to quantitative LIF measurements is based on the simplification introduced by working in the linear regime (weak-field approximation) at the expense of lower signal-to-noise ratio [28]. Under these conditions, stimulated emission is negligible and the population promoted to the excited state is directly proportional to the laser spectral irradiance, the absorption coefficient and the population in the ground state. This scheme is very well suited for radical number densities $> 10^{10}$ cm^{-3} at flame temperatures, for species with relatively large fluorescence quantum yields. For example, CH, CN and C_2 number densities have been measured in low-pressure flames [1, 2, 4] and plasmas [28, 29, 37] using this scheme. Lower number densities usually require at least partial saturation of the transition [27]. Thus, the choice of calibration method and excitation regime depends on the spectroscopic properties, expected number density and fluorescence quantum yield of the species.

CH radicals are important in the initiation step of prompt NO formation and are flame-front markers for visualizing structure. CH absolute density measurements are becoming common in low-pressure flames by either LIF [1, 2, 4] or absorption techniques [5, 6, 38, 39], but measurements in atmospheric pressure flames present specific problems related to the presence of this radical in narrow regions, and are still scarce. Besides some early estimates [26], only CRD studies by Mercier *et al.* [11] and Evertsen *et al.* [40], FM absorption measurements by Peterson and Oh [16], and LIF work by Walsh *et al.* [3] have reported absolute concentrations of the CH radical at atmospheric pressure. These studies used the A–X(0,0) or C–X(0,0) bands to find CH peak concentrations in methane/air flames of 0.6, 0.8, 2 and 4 ppm, respectively. We note that slot burners were used in the absorption experiments, to increase sensitivity from the extended pathlength of several centimeters; this also avoided much of the difficulty of spatially resolving the thin CH structure in atmospheric pressure flames.

In previous work [41], we examined the feasibility of exciting a predissociative rotational level in the CH B $v' = 1$ state via the B–X(1,0) band to obtain absolute measurements in atmospheric-pressure flames. We found that the $N' = 8$ ($\tau = 0.35$ ns) [42, 43] level was the best choice, considering the attainable signal-to-noise ratio compared to other predissociative levels, and the relatively low sensitivity of the fluorescence quantum yield to collisions. In the present paper, we report absolute peak number densities of the CH radical in the 2-ppm range measured by quasi-linear LIF exciting the B–X(1,0) band in a methane/air flame at atmospheric pressure. In related previous work, Rothe and co-workers [44, 45] have studied the dynamics of the LIF process for predissociating OH A $v' = 3$, and discuss the effects of rotational energy transfer in the ground state on the interpretation of the LIF signal. We examine here the role of rotational relaxation in the excited and ground states of CH, as well as the polarization of the fluorescence and the spatial resolution of the experiment, to obtain absolute measurements of CH at atmospheric pressure. Reliable CH number densities can be determined using this LIF scheme, if the collisional population redistribution and polarization details are properly considered

2 Experimental

The flame was a partially premixed CH_4/air Bunsen flame, burning at atmospheric pressure at an equivalence ratio of 1.36 in the premixed inner cone. The 1.65-cm-diameter premixed flow of 7.2 SLM was surrounded by a 10-cm radius of co-flow air. The CH B–X(1,0) transition at 365 nm was excited with a dye laser beam (LambdaPhysik FL-2002, temporal width $\sim$ 14 ns, spectral bandwidth 0.20 ± 0.02 cm^{-1}, vertically polarized), pumped by a XeCl excimer laser (LambdaPhysik EMG 103 MSC). Laser pulse energies between 1 μJ and 1 mJ were measured with a micro-Joulemeter (Rj-7200, Laser Precision Corp.). The beam cross section was determined with burn paper. We used two experimental configurations, one for absolute measurements and a second for flame imaging. The respective laser-beam cross sections were 0.25×2.0 mm^2 and 0.25×30 mm^2. The spectral irradiance was calculated as:

$$I = I^{\circ} \Gamma(\nu) = \frac{E \cdot \Gamma(\nu)}{\Delta\nu \tau_L A} \tag{1}$$

where E is the laser energy per pulse (J), $\Delta\nu$ is the laser bandwidth (cm^{-1}), $\Gamma(\nu)$ is the dimensionless lineshape overlap integral [46], τ_L is the laser-pulse temporal length (s), and A is the dye-laser-beam cross-sectional area (cm^2).

In the absolute LIF measurement set-up, the path of the laser beam through the Bunsen flame perpendicular to the flow was imaged with two identical spherical lenses ($f/4$, $f = 200$ mm). After passing a depolarization filter, the light was directed onto a spectrograph SPEX 270 M ($f/4$, 500-nm blaze angle) and detected with a gated intensified CCD camera (Princeton Instruments, ICCD-576G/RBT, 14 bits dynamic range, 384×576 pixels, pixel size 23 μm). The entrance slit was set to 450 μm. The fluorescence was spectrally dispersed along one direction of the array with a resolution of 1.5 nm, which was sufficient to separate CH B–X vibrational bands. The other direction in the collected images corresponded to the position along the path of the laser beam and provided spatial resolution of the fluorescence images. The images shown in the figures have a horizontal spectral axis and a vertical spatial axis. One CCD pixel corresponds to 20 μm in the flame, but the imaging of a test card indicated that the spatial resolution of our optical collection system was approximately 25 pixels or 500 μm, influenced mostly by the lenses and spectrometer. Appropriate background images of the dark current of the CCD camera and of the natural emission of the flame were recorded and subtracted from the dispersed

fluorescence images. The gate of the image intensifier was set to 200 ns; wide enough to include any excimer laser jitter and short enough to minimize the subtracted optical-flame emission. For polarization measurements, the laser light was vertically polarized. To filter the fluorescence at either 0° or 90° polarization angle, polarizer sheets were positioned after the collection lenses and rotated accordingly.

The flame visualization configuration imaged the fluorescence with an UV-Nikon lens ($f/4.5$, $f = 105$ mm) through a KV-380 filter (Schott), and two-dimensional fluorescence images were detected on the CCD. The filter minimized interference from Rayleigh scattering of the laser pulse and isolated fluorescence from the CH B–$X(0,0)$, (1,1) and A–X bands. The resolution for this imaging arrangement was approximately 150 μm (∼ 3 pixels).

3 Method

Laser-induced fluorescence using a laser pulse with a temporal length (τ_L) longer than the fluorescence lifetime (τ_{Fl}) is usually described by the steady-state approximation during the laser pulse. Atmospheric-pressure flames studied with nanosecond lasers are good examples of such systems because collisional rates are fast enough to compete with laser excitation. The time-integrated laser-induced fluorescence signal, assuming instantaneous steady state and accounting for delayed fluorescence (decay time τ_{Fl} after the laser) if necessary, is:

$$S_{\mathrm{LIF}} = A_{21} n_2 \left(\tau_L + \tau_{\mathrm{Fl}}\right) F_{\mathrm{Fl}} K \tag{2}$$

where A_{21} is the total emission coefficient between the upper and the ground levels, n_2 is the steady-state number density in the upper state, F_{Fl} is fraction of fluorescence collected, and K is an experimental constant containing geometrical and detection electronics factors. The populations in the ground state and excited states must be modeled. We will follow the work of Rothe *et al.* [44, 45, 47] and Bormann *et al.* [48] by dividing the excited state into two levels to account for optically and collisionally populated levels in the rotational manifold. Populations are denoted by n_{2a} and n_{2b}, respectively. The excited state levels are deactivated by emission A_{21}, predissociation (P_2) and quenching (Q_2) The net rotational relaxation (RET) (R_1) into the ground-state rotational level is proportional to the difference between the initial density in the ground-state pumped level n_1^0 and the steady-state number density n_1. For simplicity, in the excited state we consider the rotational transfer R_2 to be a net transfer rate from $n_{2a} \rightarrow n_{2b}$. The coupled differential equations are:

$$\begin{aligned}
\frac{\mathrm{d}n_1}{\mathrm{d}t} &= BI(n_{2a} - n_1) + \left(n_1^0 - n_1\right) R_1 \,, \\
\frac{\mathrm{d}n_{2a}}{\mathrm{d}t} &= BI(n_1 - n_{2a}) - n_{2a} L \,, \\
\frac{\mathrm{d}n_{2b}}{\mathrm{d}t} &= n_{2a} R_2 - n_{2b}(A_{21} + Q_2 + P_2) \,,
\end{aligned} \tag{3}$$

where n_1^0 is the initial population in the pumped level of the ground electronic state. L is total depopulation rate of the level n_{2a}, including emission (A_{21}), quenching (Q_2), predissociation (P_2) and rotational energy transfer (R_2) : $L = A_{21} + Q_2 + P_2 + R_2$. At atmospheric pressure, $L \gg A_{21}$, but we include emission in the equation for the sake of completeness. Applying the steady-state approximation:

$$n_1 = \frac{n_1^0 R_1}{R_1 + \frac{LBI}{L+BI}} \tag{4}$$

$$n_{2a} = \frac{n_1^0 BI}{BI\left(1 + \frac{L}{R_1}\right) + L} \,. \tag{5}$$

Rothe *et al.* [44] have shown the steady-state approximation to be an appropriate description of the system at atmospheric pressure.

If $L \gg BI$ then $n_{2a} = n_{2a}^L = n_1^0 BI/L$. The total population $n_2 = n_{2a} + n_{2b}$

$$\begin{aligned}
n_2 = n_{2a}\left(1 + \frac{R_2}{A_{21} + Q_2 + P_2}\right) &= \frac{n_{2a}^L}{\frac{BI}{L}\left(1 + \frac{L}{R_1}\right) + 1} \\
&\times \left(1 + \frac{R_2}{A_{21} + Q_2 + P_2}\right) \,.
\end{aligned} \tag{6}$$

The fluorescence quantum yield for the two-level excited state is expressed by

$$\Phi_{\mathrm{Fl}} = \frac{A_{21}}{L}\left(1 + \frac{R_2}{A_{21} + Q_2 + P_2}\right) \,. \tag{7}$$

The final expression for the LIF signal is very similar to the one obtained for weak excitation with no competitive collisions, and if $L \gg BI$, the term in the denominator (accounting for the stimulated-emission feedback, RET repopulation of the ground state and relaxation of the excited state) will be equal to unity.

$$S_{\mathrm{LIF}} = \frac{n_1^0 BI}{\frac{BI}{L}\left(1 + \frac{L}{R_1}\right) + 1} \Phi_{\mathrm{Fl}} (\tau_L + \tau_{\mathrm{Fl}}) F_{\mathrm{Fl}} K \,. \tag{8}$$

The model analysis assumes steady state populations (4) and (5) to describe the response of the LIF signal (8) to variations in the pumping rate (BI) for the CH B–$X(1,0)$ predissociative level excitation scheme. We used the parameters of the current experiment, with a maximum pumping rate BI of $1.5 \times 10^9\ \mathrm{s}^{-1}$, equivalent to a laser energy of 25 μJ/pulse exciting the $Q_1(8)$ line, or 50 μJ/pulse exciting either $R_1(7)$ or $P_1(9)$ lines. Collisional rates for CH B have been discussed previously [41] and are summarized in Table 1. Rotational relaxation in the ground state is assumed to be equal to the relaxation rate of the excited state. For the ground state, exchange rates between lambda doublet components are assumed to be fast, and transfer between spin-orbit levels $F_1 \leftrightarrow F_2$ unlikely [49].

The ground-state steady state was not perturbed to any great extent, because at the pumping rate of $6 \times 10^8\ \mathrm{s}^{-1}$ we conserved 85% of the initial density (Fig. 1, upper panel). However, a better descriptive quantity is the pumping ratio [44] PR, $PR = (n_2/n_1^0) L \tau_L$, which gives the number of times the ground-state rotational level population has been

Measurement/model parameters	Values
E_{min} (μJ)	1
E_{max} (μJ)	20
Laser cross section (cm^2)	0.03×0.2
Laser pulse length FWHM (ns)	14
Laser bandwidth FWHM (cm^{-1})	0.20 ± 0.02
Overlap integral (1900 K) $B\ v' = 1\ N' = 8$	0.45 ± 0.06
F_{fl}	0.52
B ($m^2\ J^{-1}\ s^{-1}$)	4.5×10^9, 2.2×10^9 ($Q_1(8.5)$, $R_1(7.5)$)
$A_{21}(v' = 1, N' = 8)$ (s^{-1})	2.2×10^6
P_2 ($v' = 1$, $N' = 8$) (s^{-1})	2.9×10^9
Q_2 (s^{-1})	4.2×10^8
R_2/Q_2	$8 - 10$
Fluorescence quantum yield	0.00085 ± 0.0001
Temperature (K)	1900 ± 100
F_B ($v'' = 0$, $N'' = 8$, $J = 8.5$, A) at 1900 K	0.0193
F_B ($v'' = 0$, $N'' = 7$, $J = 7.5$, A) at 1900 K	0.0203
N_2 Raman cross section at 366.5 nm (cm^2)	2.43×10^{-30}

TABLE 1 Parameters used in the model and in the absolute measurements of CH via B–X(1,0) band excitation of the $N' = 8$ predissociative level, collecting light in the B–X(1,1) band

depleted by laser excitation. For the $R_1(7)$ and $Q_1(8)$ lines ($B(Q(8))I = 6 \times 10^8\ s^{-1}$ for 10 μJ/pulse), the population pumping rates are three and six, respectively (Fig. 1, lower panel). At flame temperature, 1900 K, the initial fraction of molecules in the $N'' = 8$ (F_1 or F_2) ground-state rotational level was approximately 4%. Assuming that rotational transfer was much faster in the optically pumped ground-state spin-orbit manifold, the model indicates that 12% to 24% of the total population in the ground state F_1 spin-orbit manifold was depleted at the maximum laser power of our experiment. This is a significant fraction of the total population, and several times the initial population in the excited level. Rothe *et al.* [44] point out that a model with a high pumping ratio is not sustainable and must break down when sufficient population is moved and the ground manifold can no longer be considered a bath-state of constant population. A second factor, not discussed in the Rothe model, is the contribution of chemical production pathways in repopulating the ground state. For OH $X^2\Pi$ the chemical production replacement rate estimated from the flame kinetics models is in the $10^7\ s^{-1}$ range, and it is reasonable to discard this path. However, it is known that the ground state of CH, unlike may other molecules, reacts as quickly as the collisional removal of the excited states [50], and as flame models show, chemical production and loss rates are in the 10-ns range at atmospheric pressure, and may contribute to repopulating the perturbed ground-state levels during the laser pulse. This additional replacement effectively extends the range of excitation pulse energies where the model is a realistic approximation. In principle, one could even derive chemical rate information in flames at reacting flows from modeling the signal at very high power; this would be especially feasible at elevated pressures. Collisional quenching of the CH excited state could also repopulate the ground state, causing similar effects. Furthermore, the level distributions from such chemical production steps are uncertain and not necessarily thermal. We recommend estimating the pumping rate before making quantitative measurements, and keeping the laser intensity in a regime where only a moderate amount (< 20%) of the total ground population is excited, in order to avoid model breakdown.

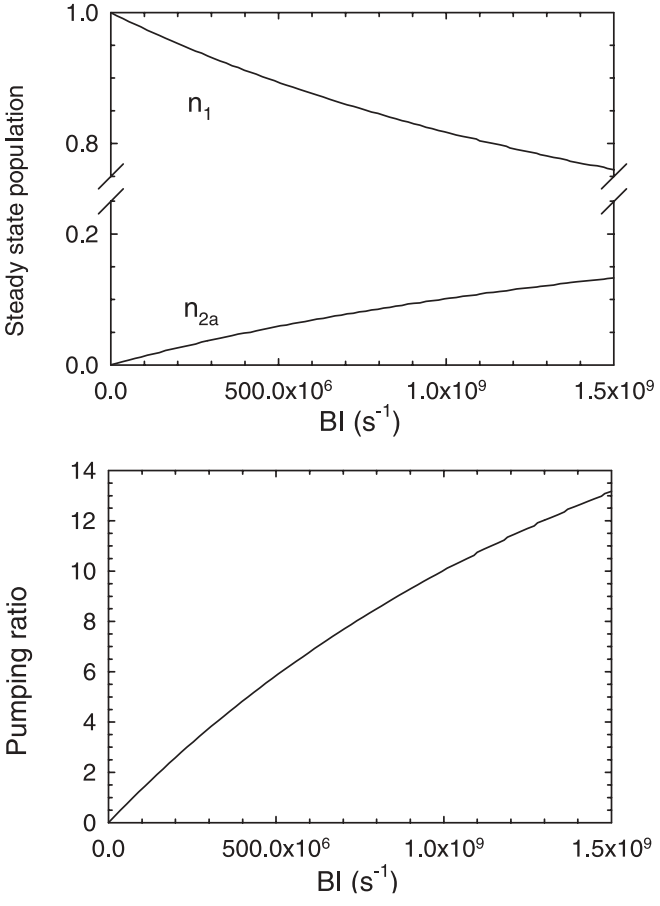

FIGURE 1 LIF Model results for CH B–X(1,0) excitation for $R(7)$, $Q(8)$ and $P(9)$ lines. The energy for the optical pumping rate scale varies from 0 to 25 μJ for $Q(8)$. Scaling to $R(7)$ and $P(9)$ is $B_{P(9)\text{ or }R(7)}I = 0.5B_{Q(8)}I$. *Upper panel*: steady-state populations for the ground and excited states as a function of the pumping rate. *Lower panel*: pumping ratio (see text) versus optical pumping rate

The simple linear model versus pumping rate (8) with denominator equal to one) and the complete model with time-varying population (8) are compared in the upper panel of Fig. 2. At low pumping rates, $BI < 6 \times 10^8\ s^{-1}$, the model behavior is linear. The deviation from linearity is noticeable only at high pumping rates, where it corresponds also to large differences between the initial population and steady-state

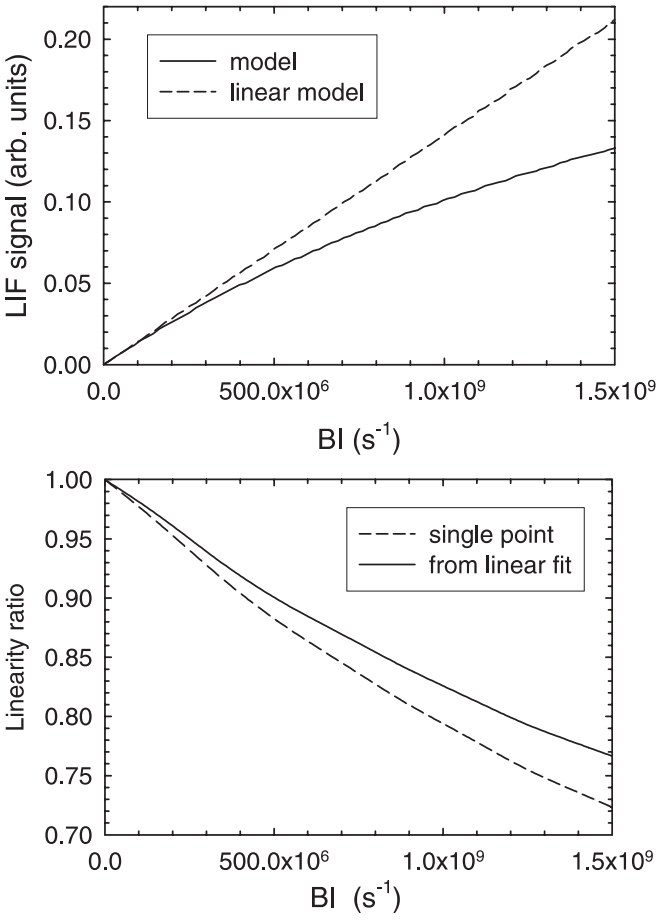

FIGURE 2 *Upper panel*: LIF model results for CH B–$X(1,0)$ excitation. *Lower panel*: deviation from the low-power linear regime versus pumping rate. The deviation determined by the linear slope (*solid line*) of the simulated signal from $BI = 0$ to the given energy value is smaller than the deviation at that single laser energy (*dashed line*)

ground-state population (Fig. 1). The ratio of the linear model and the predictions of (8) is shown in the lower panel of Fig. 2, and is used to correct experimental results in Sect. 4 of this paper. The ratio is presented in two different ways. The correction labeled 'single point' and shown by the dashed line refers to the simple ratio of signal to linear value at a given pumping rate. In most experiments, however, we measured the LIF signal at different laser powers and fitted the resulting set of points to a line. The slope usually showed no clear deviation from linearity, as is the case here, and was directly used in the analysis. The second plot (Fig. 2 bottom, solid line) mimics this procedure, where the ratios were determined by dividing the slope from the linear fit of LIF signal for laser pulse energies below the given pumping ratio by the linear (extrapolated, low-power) LIF signal at this pumping rate. This gave the slope ratio as a function of the last point or highest pump power. At low pumping rates, this ratio was very close to unity. Only for energies above 20 μJ (Q-line pumping) was the slope 20% smaller than that derived for perfectly linear pumping. Analysis of the LIF model in (8) showed a linear regime at laser powers above the weak-field approximation ($PR \ll 1$), and saturation effects with deviations larger than 20% only appeared for the present LIF scheme at pumping ratios $PR \gg 10$. This quasi-linear LIF regime requires fast replenishment in the ground-state level and a fast loss rate in the excited state to compete efficiently with optical pumping.

The model can be extended to high pressure for excitation with the same nanosecond laser pulse. At elevated pressure, the CH $B\ v' = 1\ N' = 9$ which has a lifetime of 75 ± 10 ps [43] can be used instead of the CH $B\ v' = 1\ N' = 8$ (lifetime of 350 ps) to minimize quenching effects. For example, at a pressure of 10 atm, the collisional relaxation rates are ten times larger than those at 1 atm. Competition between optical pumping and collisional processes provides an approximately linear LIF excitation range for laser pulse energies an order of magnitude larger than at 1 atm. Unfortunately the pumping ratio increases with laser power and if we ignore depletion of the entire lower-state manifold, the pumping ratio approaches values as large as 100. Such a value corresponds to several times the total ground-state population of CH, and obviously this pressure increase in pumping ratio only applies if there is fast chemical production of the CH ground state, or if rapid collisional quenching repopulates the ground state. At low pressure, RET refilling of the ground-state level is slow and the scheme saturates at lower power. Fluorescence signal levels are also lower, hence in our low-pressure flame excitations we pumped the longer lived CH $B\ v' = 1\ N' = 7$ level instead [32]. Excitation with picosecond laser pulses at atmospheric and lower pressures will not produce linearly increasing LIF signals even at modest pumping ratios because the pulse length is much shorter than the collisional relaxation times. For picosecond laser excitation, ground-state refilling by RET is significant only at elevated pressures of 10 atm.

Walsh *et al.* [3] determined the CH number density from CH A–$X(0,0)$ LIF excitation in an atmospheric methane diffusion flame, using a linear LIF interpretation of the signal similar to that employed rigorously in low-pressure experiments [1]. Implementing the model in (8) with appropriate experimental, collisional and spectroscopic parameters, their pumping ratio for 1 μJ/pulse was about 0.5. The deviation from ideal linear behavior was $\leq 3\%$ in that experiment, so their model is a realistic representation of the LIF signal in that laser power regime.

Rothe *et al.* [45] have shown at atmospheric pressure that the LIF signal following excitation of a predissociative level is proportional to local variations of concentration and relaxation rates in the ground state. OH measurements are especially affected because this radical is present in all flame regions at a wide variation of temperatures, compositions and collisional rates. In OH $A\ v' = 3$, $P \sim 1.3 \times 10^{10}\ \mathrm{s}^{-1}$, $Q + R \sim 2 \times 10^9\ \mathrm{s}^{-1}$ and the steady-state populations at very high laser powers depend on the rotational relaxation rate in the ground state, (4) and (5). The CH B case is different because predissociation and collisional rates are quite similar ($P \sim 3 \times 10^9\ \mathrm{s}^{-1}$, $Q + R \sim 4 \times 10^9\ \mathrm{s}^{-1}$), and thus collisional effects in the excited state are minimized but cannot be neglected. Laser powers in the present scheme were lower than normally used in the OH $A\ v' = 3$ experiment, avoiding large differences between the initial population in the ground state and the steady-state population.

We may speculate that the steady-state CH excitation fraction may still vary due to local variations in rotational relaxation rates. CH is present in regions between 1000 and 2000 K. Q has been observed to increase about 40% in this

temperature range. We find that a 40% variation in both Q and RET would make at most a 10% difference in the modeled LIF signal if the pumping ratio is relatively high, $PR \sim 10$. An increase in excited-state population because of RET redistribution in the ground state is compensated by additional quenching (assisted by RET) in the excited state. Effects of variations in the flame collisional environment on the steady-state population of the optically excited state are not noticeable. As the laser power decreases, RET level refilling is less important. Under quasi-linear conditions $PR \sim 1$, and the denominator in (8) is weakly dependent on collisions. LIF images taken in this excitation regime only require correction for possible fluorescence quantum yield variation to provide absolute concentration measurements. Interestingly, the range of corrections due to variation in collisional rates with temperature and composition may be larger here than in the high-optical-pumping regime. Because the detailed temperature and composition variations of RET in the ground and excited states are not well known, quantitative corrections to the LIF signals are not available. For high optical excitation rates beyond the scope of this study, the LIF signal should depend largely on ground-state RET.

4 Results and discussion

4.1 CH *B–X*(1, 0) *laser-induced fluorescence*

The fluorescence from CH B–X(1,0) excitation is readily detected, as seen in Fig. 3. In this spectral region, there is overlap with the CH_2O A–X 4_1^0 band [51, 52]. This accidental overlap was advantageous for detecting both CH and CH_2O using the same experimental set-up [32, 51]. The flame structure is such that the spatial overlap between CH and CH_2O is small, and measurements free from interference are readily obtained by subtracting the off-resonance background. Figure 3 shows clearly differentiated spatial regions for CH and CH_2O. The qualitative spatial profiles in the upper section of the panel display the CH LIF with some CH_2O signal from the continuous background and Rayleigh scattering in the flame inner cone. This spectrum was taken at relatively high laser power, where CH LIF is saturated but CH_2O LIF is not. Later CH PLIF images were taken in the linear excitation regime, increasing the ratio of CH versus CH_2O signals and thus providing better spatial discrimination of the two signals.

Figure 4 contains a broader spectral region of CH LIF excitation taken near the peak of the CH distribution. It shows predissociated levels in the R branch ($N' > 6$). Simulations of the excitation LIF spectra show good agreement when predissociation, rotational relaxation and quenching effects are

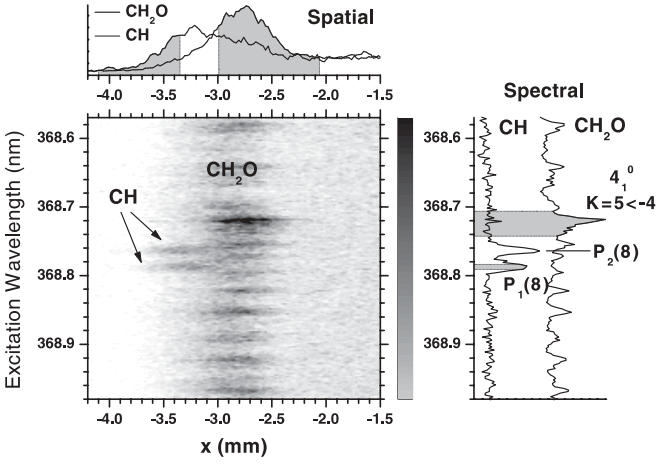

FIGURE 3 Excitation scan showing CH, CH_2O, and scattering in the flame front of the partially premixed section of the Bunsen flame. Axes in the composite image are laser excitation wavelength (*vertical*) and radial distance to the burner axis (*horizontal*). Fluorescence is collected using a cut-off filter to minimize Rayleigh scattering before the spectrograph and CCD camera. The right plot shows the spatially resolved LIF excitation scans after integrating the sections between 3.5 and 4.0 mm (CH) and 2 and 3 mm (CH_2O). The upper plot shows the spatially resolved distributions after integrating the CH B–X(1,0) $P_1(8)$ line and the bandhead of the CH_2O A–X 4_1^0 R branch

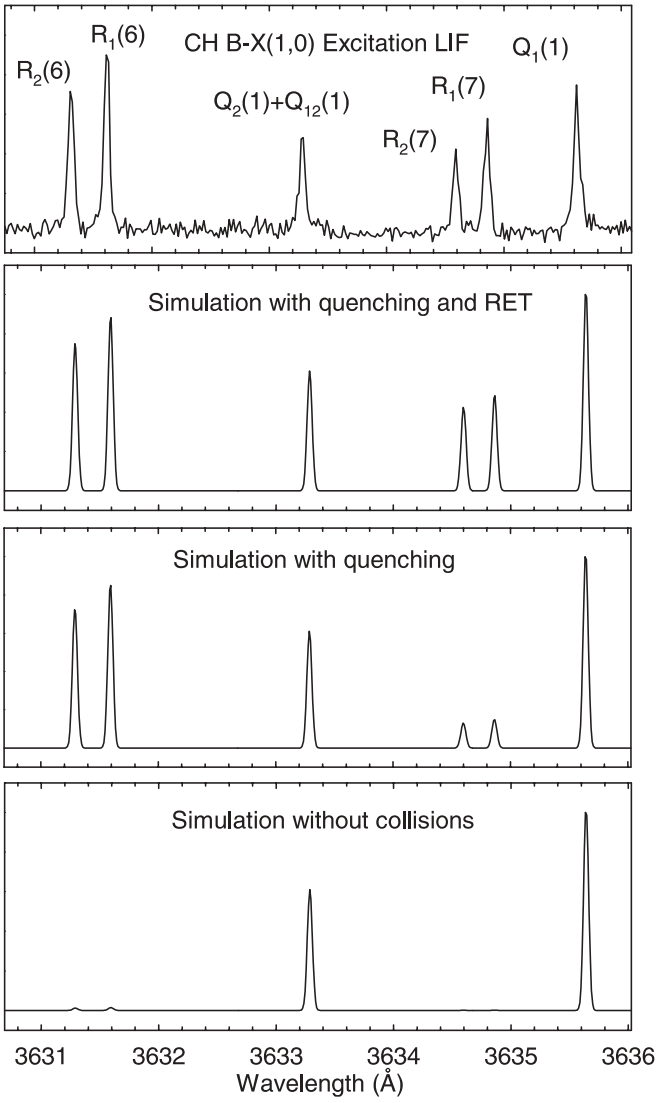

FIGURE 4 *Upper panel*: LIF intensity versus laser wavelength for CH B–X(1,0) in the flame front at $T = 1900$ K, laser energy $= 50\,\mu$J/pulse ($\sim 4 \times 10^6$ W cm^{-2}/cm^{-1}) along with simulations generated by LIFBASE [57] using a temperature of 1900 K and a Gaussian lineshape with a bandwidth of 0.35 cm^{-1} FWHM. *Lower panel*: simulation without any collisions; predissociation rates are from Elander's work [42]. *Center lower panel*: simulation with predissociation and collisional quenching rate $Q = 4 \times 10^8$ s^{-1}. *Center upper panel*: simulation including predissociation, quenching and rotational relaxation. Fluorescence quantum yields including rotational relaxation effects are from Luque *et al.* [41]

included (Fig. 4, middle panels). In the absence of collisions, signal levels for the $R(7)$ line, one of those selected for absolute measurements, is barely visible (Fig. 4 lower panel). The experimental spectrum was taken at power levels near partial saturation of the R transitions. Some lines belonging to the Q branch ($N' = 1$) have higher absorption coefficients and do not predissociate. Their greater likelihood of saturation explains the slight difference between simulated and calculated Q and R line intensities. Broadening in Q lines is not more than $0.07\,\mathrm{cm}^{-1}$ beyond the expected bandwidth of $0.35\,\mathrm{cm}^{-1}$ from simulated spectra, showing that power saturation is quite moderate.

Dispersing the fluorescence from either $R_1(7)$ or $Q_1(8)$ excitation produces the spectra in Fig. 5. Even for a level with a predissociation lifetime of 0.35 ns, collisions are competitive and we observe emission from many CH levels in addition to the excited one. The spectrum is strongly influenced by collisional rotational, vibrational and electronic energy transfer. The contribution to the fluorescence signal intensity from vibrational energy transfer to $B\ v' = 0$ and electronic transfer to the A state for a time-integrated signal is

$$I = n_{\mathrm{B1}}\Phi_{\mathrm{B1}}\left(1 + \frac{1}{A_{\mathrm{B1}}}(k_{\mathrm{v}}\Phi_{\mathrm{B0}} + k_{\mathrm{e}}\Phi_A)\right) \tag{9}$$

where k_{v} and k_{e} are the corresponding vibrational and electronic transfer rate constants, which have been measured previously [41], n_{B1} is the population excited to CH $B\ v' = 1$ and Φ_ι are the fluorescence quantum yields for the corresponding levels. Quantitative analysis of the spectrum shows that about 50% of the light originates from CH $B\ v' = 0$ and CH A states, independent of the initial excited rotational level. The total signal can be reduced by the predissociation term in the quantum yield, Φ_{B1}. There is less collisional transfer to other levels when the predissociative CH $B\ v' = 1$, $N' = 8$ is excited, compared to pumping lower rotational levels, but the ratios of fluorescence from B–$X(1,v'')$ and the collisionally transferred $B(v' = 0)$ and A state populations remain the same for predissociative and non-predissociative levels since the various energy transfer constants do not vary significantly with rotational number, as seen previously [41].

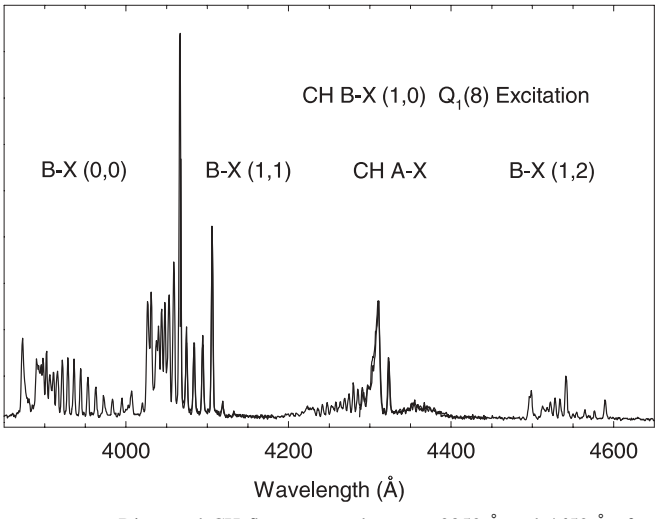

FIGURE 5 Dispersed CH fluorescence between 3850 Å and 4650 Å after excitation of the B–$X(1,0)$ $Q_1(8)$ line. Resolution is 2.5 Å (FWHM). This is the typical fluorescence collection range in CH 2-D LIF images

To maximize the collection of fluorescence signal, a typical requirement for 2-D LIF images, emission from CH A–X at 430 nm should be included. The fluorescence yield from levels populated by energy transfer does not have a larger variation with temperature or composition than the collisional quenching in the initially excited $B(v' = 1)$, so it is reasonable to collect this contribution in fluorescence 2-D images. For absolute CH measurements, we used only the signal from B–$X(1,1)$, to simplify the analysis, at the expense of the overall signal magnitude and thus signal-to-noise ratio. Moreover, the spectrograph used could only capture either B–$X(0,0)$ or A–X in combination with B–$X(1,1)$ in a single spectrum (Fig. 5 is a composite of two spectra with a common overlapping section).

4.2 CH *absolute number density determination*

To determine absolute concentrations from relative LIF via Rayleigh or Raman scattering calibrations, one must precisely determine the laser spectral irradiance, emission and absorption spectroscopic coefficients, and the fluorescence quantum yield. Polarization of the fluorescence and spatial resolution effects must be correctly evaluated, as well as the collisional and saturation effects just discussed. State variables such as temperature and pressure are needed. The former can be measured by non-intrusive optical techniques, and for the present flame has been determined by LIF to be 1900 ± 100 K at the region where the absolute measurement was performed [53].

4.2.1 Lineshape overlap integral. Calculation of the effective spectral irradiance in (1) requires careful evaluation of the interaction between the laser and the spectroscopic transition. The lineshape overlap integral $\Gamma(\nu)$ in (1) is calculated from the convolution of the laser spectral profile, assumed to be Gaussian, and the Voigt profile of the excited CH B–X rotational line.

There are no direct data about pressure broadening for CH B–X. Dean and Hanson [54] used data from OH and NH to model CH A–X and C–X absorption, and these gave approximately $0.035\,\mathrm{cm}^{-1}$ at 1900 K. Takubo *et al.* [55] used $0.07\,\mathrm{cm}^{-1}$ for CH A–$X(0,0)$ in a propane/air flame, based on emission measurements. Finally, an examination of the CH A–X spectra by Peterson and Oh [16] taken with a near-ultraviolet diode laser in an atmospheric flame suggests collisional broadening $< 0.1\,\mathrm{cm}^{-1}$ as well. We can estimate CH B–X collisional broadening from collisional data in flames, assuming both excited (f) and ground states (i) have similar depopulation rates (k), and that elastic collisions are not important [56]:

$$\Gamma_c = \frac{k_i + k_f}{2\pi c}\,. \tag{10}$$

The CH B quenching rate estimated in this flame was approximately $\sim 4 \times 10^8\ \mathrm{s}^{-1}$ and the total rotational relaxation was about eight- to ten-times faster than quenching in the B state of CH in flames [57]. The total depopulation rate for CH B–X

$Q(8)$ was thus estimated to be $1.2 \times 10^{10}\,\mathrm{s}^{-1}$. We obtained a value of approximately $0.06\,\mathrm{cm}^{-1}$ for collisional broadening, very similar to the literature values for other CH electronic transitions. There was another homogeneous contribution to the linewidth of $0.015\,\mathrm{cm}^{-1}$ from predissociation. The inhomogeneous contribution to the Voigt profile is given by the Doppler broadening; for CH at 365 nm and $T = 1900\,\mathrm{K}$, $\Delta\nu_\mathrm{D} = 0.235\,\mathrm{cm}^{-1}$. The convolution of this absorption profile and the laser lineshape gave a final bandwidth for the observed transition of approximately $\sim 0.35\,\mathrm{cm}^{-1}$. The lineshape overlap integral at the center of the absorption line was 0.45 ± 0.06 or $g(\nu) = \Gamma(\nu)/\Delta\nu = 2.30\,\mathrm{cm}$.

4.2.2 Fluorescence quantum yield. Determination of the fluorescence quantum yield is a critical step to performing quantitative LIF. The excited level in CH $B\ v' = 1$, $N' = 8$ shows unusual behavior because of the unique combination of predissociative and collisional relaxation rates for this level at atmospheric pressure in a flame. We have devoted a full-length paper to the study of energy transfer from $B\ v' = 1$ and fluorescence quantum yield modeling [41]. In a brief description, the fluorescence quantum yield is calculated after solving the system of coupled equations describing the dynamics of all the excited-state rotational levels:

$$\frac{\mathrm{d}n_i}{\mathrm{d}t} = -(A_i + Q_i + P_i)n_i + B_{ki}I(t)n_k + \sum_{i\neq j}(R_{ji} - n_j - R_{ij}n_i) \tag{11}$$

R_{ij} are the state-to-state rotational relaxation rates and $B_{ki}I(t)n_k$ is the optical pumping term which is different from zero only for the excited rotational level. The fluorescence quantum yield after pumping the rotational level i is:

$$\Phi_i = \frac{\int_0^\infty \sum_i n_i(t)A_i\,\mathrm{d}t}{\int_0^\infty \sum_i n_i(t)(A_i + Q_i + P_i)\,\mathrm{d}t} = \frac{\int_0^\infty \sum_i n_i(t)A_i\,\mathrm{d}t}{n_T} \tag{12}$$

n_T is the population optically pumped from the ground state level k to the level i in the excited state. We evaluated the uncertainty of the fluorescence quantum yield by modeling experimental variability. The model has several parameters: quenching, rotational relaxation, emission and predissociative rates, which all have experimental errors (see Table 1). To test the overall effect of these experimental uncertainties we varied the input parameters randomly ±10%, and the average fluorescence quantum yield was 0.00085 ± 0.00010. This is very similar to the previously published value of 0.00092 [41].

Figure 4 displays R-branch flame excitation spectra for $B\ v' = 1\ N' = 7$ and 8, which in the absence of predissociation should have the same intensity. The $B\ v' = 1\ N' = 7$ level has a collision free lifetime of 4.5 ns and $B\ v' = 1\ N' = 8$ is 0.350 ns [42]. Without collisions, the ratio of LIF between the two doublets should be approximately 13. Adding the quenching to the fluorescence quantum yields predicts this ratio should be five, still far from the ratio of two, observed experimentally. Including rotational relaxation in a dynamic model decreases the predicted ratio to approximately two, in excellent agreement with observations, as shown in the figure. As this model shows, rotational relaxation lowers the fluorescence quantum yield of weakly or non-predissociative levels like $N' = 7$ by promoting molecules to fast predissociative levels with higher rotational quantum number. Conversely, collisional transfer to lower rotational levels below the predissociative threshold increases the fluorescence quantum yield of predissociative levels like $N' = 8$.

4.2.3 CH *B–X spectroscopic coefficients.* Radiative and absorption coefficients were taken from the LIFBASE database [58]. The CH B–$X(1,0)$ spectroscopic coefficients and CH B lifetimes have been computed using verified electronic transition moments and rovibrational RKR wave functions [59]. Spectroscopic coefficients for CH A–$X(0,0)$ and B–$X(0,0)$ have an error of less than 5% using this method. However, comparison with the CH $B\ v' = 1$ experimental lifetimes measured by Brozozowski *et al.* [60] and Wang *et al.* [61] suggests that the lifetimes and absorption coefficients for $B\ v' = 1$ might be in error by as much as 10%. For example, Wang et al. obtain an average lifetime for CH $B\ v' = 1$, $N' = 1 - 6$ of 419 ± 23 ns, versus an averaged value of 460 ns from LIFBASE. A CRD experiment [32] comparing CH concentrations measured in a low-pressure flame with both B–$X(1,0)$ and B–$X(0,0)$ bands suggests the error in the spectroscopic coefficients for CH $B\ v' = 1$ is likely less than 10%.

CH LIF images and absolute density determinations collect different fractions of the fluorescence. For the LIF images, all the emission to the red of the B–$X(1,0)$ excitation wavelength is collected, including the vibrational transfer to B–$X(0,0)$ and the electronic transfer to CH A–X. The absolute concentration measurements are limited to emission from the B–$X(1,1)$ band, which accounts for 52% of the fluorescence from the excited level $B\ v' = 1$ [59, 62].

4.2.4 Calibration of the LIF signal. Off-diagonal excitation/detection LIF schemes applied to combustion diagnostics are well suited for Raman signal calibration because the calibration and LIF signals can be in the same spectral region [1]. In the case of CH B–$X(1,1)$ detection, Raman and LIF can be spatially and spectrally resolved easily using an imaging spectrograph. In the partially premixed flames studied here, the feedstock gases and flame reacting zones were located close together, making feasible simultaneous collection of spatially resolved LIF and calibration Raman signals. Figure 6 shows an example image recorded at 14 mm height above the burner surface. The horizontal axis corresponds to wavelength and the vertical axis corresponds to the radial distance from the center of the flame, parallel to the burner surface. The LIF from CH B–$X(0,0)$ and B–$X(1,1)$ appears in the same image as the Raman signals from O_2, N_2 and CH_4. CH_4 and O_2 are consumed in the flame and disappear in the flame front. The N_2 signal is persistent, but weakened by the decrease in number density due to the temperature gradient through the flame front. One concern about this approach is the possible effect of heated reactants in the pre-flame region, which would alter the calibration. We found the N_2 Raman signal was constant (within uncertainty limits) with and without the flame ignited (Fig. 7), thus assuring that the unburned interior gas temperature was 298 K, and thus, the feedstock in the center of the

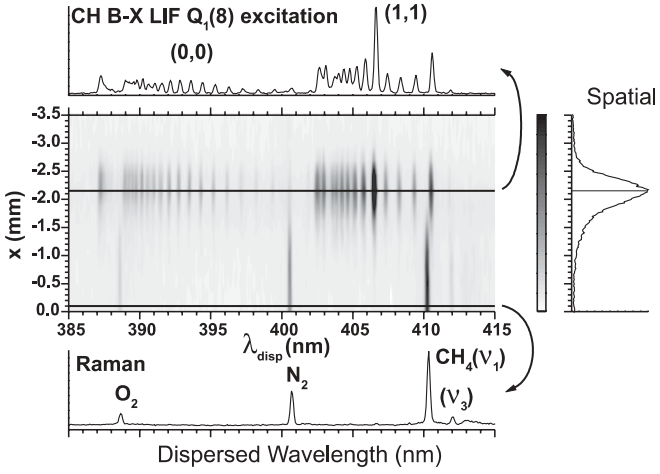

FIGURE 6 Spectrograph image taken after CH B–X(1,0) $Q_1(8)$ excitation in the premixed zone of the Bunsen flame at a height of 14 mm above the burner. The abscissa is fluorescence wavelength (resolution 2.5 Å FWHM), and the ordinate is the radial distance to the flame center. The *image* shows only the *left-hand side* of the flame for simplicity. The *upper* and *lower plots* show spectra at the center of the premixed flame front, and at the center of the area containing the unburned reactant mixture. Raman signals from O_2, N_2 and CH_4 are easily identified in the reactant mixture. LIF from CH B–X(1,1) and (0,0) bands appears in the flame front. The *right plot* shows the spatial distribution of CH integrating the B–X(1,1) R- and Q-branch fluorescence. The width (largely instrumental, see text) is approximately 600 μm (FWHM). Absolute measurements integrate the B–X(1,1) band in a width of 0.1 mm. The N_2 Raman is integrated in a width of 1 mm (from x = −0.5 to 0.5 mm in the image)

flame cone provides a well-defined calibration mixture. The partial pressure of N_2 is calculated from the mole fraction in the feedstock gases. It is well known that laser polarization determines the spatial distribution of scattering signal, which we maximized by using a vertical polarization. Calibration was performed using the N_2 Raman signal, which was large and not subject to reactive attenuation in the flame. The N_2 Raman cross-section ($d\sigma/d\Omega$) at 365.5 nm is from Eckbreth [18], and the Raman signal [1, 18] is given by:

$$S_{\text{Raman}} = \frac{P_{N_2} E}{hc\nu_{\text{Raman}}} \left(\frac{\partial\sigma}{\partial\Omega}\right) 4\pi K \tag{13}$$

where K is the same geometrical and detection constant used in (2), and was determined from the slope of the Raman signal in Fig. 7.

The LIF signal for the concentration determination was collected after exciting $Q_1(8)$ (or $R_1(7)$), while monitoring only the B–X(1,1)-band fluorescence. The slope of the plot of signal versus laser power was analyzed. The linearity of the signal is good for energies below 20 μJ, in agreement with the model in Fig. 2. The signal-to-noise ratio is too low to permit observation of small deviations from linearity. We corrected the experimental slope following Fig. 2 (lower panel). We measured concentrations exciting the $R_1(7)$ line. The main difference is that the absorption coefficient for $R_1(7)$ is about half than that for $Q_1(8)$, and thus the $R_1(7)$ excitation was less susceptible to saturation effects. Polarization effects will also be different for each branch. Concentrations from the two lines differed by < 10%. Saturation and polarization effects must therefore be small.

4.2.5 Polarization effects. Doherty and Crosley [63] first discussed polarization of fluorescence in the context of combustion diagnostics. Recent combustion-related studies have analyzed this effect, especially in studies of energy transfer processes because the measured populations can be influenced by the degree of polarization [44, 45, 64–66]. All these studies were performed for the OH A–X transition. The degree of polarization of the fluorescence is defined by:

$$P = \frac{I_{\parallel} - I_{\perp}}{I_{\parallel} + I_{\perp}} = \frac{I_{\text{v}} - I_{\text{h}}}{I_{\text{v}}} \tag{14}$$

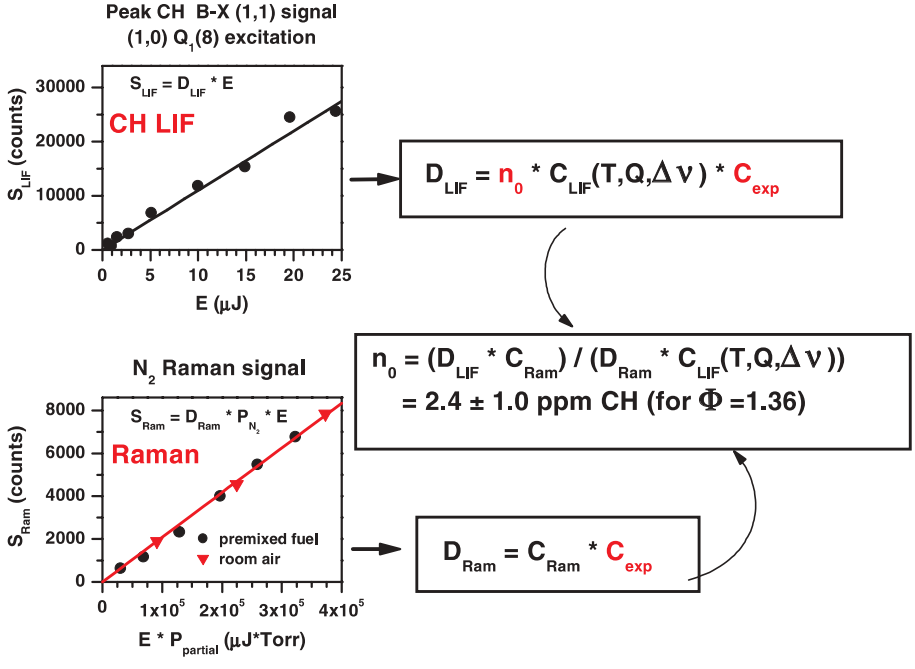

FIGURE 7 CH LIF and N_2 Raman integrated signals versus laser energy. Linearity is observed in both cases. The *right-hand side* shows how the LIF and calibration slopes (D_{LIF}, D_{Ram}) are related to obtain the CH number density. D_{LIF} is proportional to the CH number density (n_0), C_{LIF} includes fluorescence quantum yield, overlap integral, and fractional populations, and C_{exp} is the optical collection and electronic factors. The Raman slope D_{Ram} is proportional to the Raman cross section and excitation wavelength, and the same optical collection and electronic factors. The ratio of both slopes eliminates the unknown C_{exp}. The final concentration after the LIF model and spatial corrections is 2.4 ± 1.0 ppm at 1900 K and 1 atm

I_v and I_h refer to vertical and horizontal polarizations of the laser with respect to the plane of the optical table. The measured fluorescence can be separated into components polarized perpendicular ($I_\perp$) and parallel ($I_\parallel$) to the polarization of the laser beam. In the case of excitation with the laser vertically polarized, $I_v = I_\parallel + I_\perp$. For horizontal polarization, $I_h = I_\perp + I_\perp$. The total fluorescence signal corresponds to the summation over the three axes, $I_{iso} = I_x + I_y + I_z = 2I_v + I_h$, equivalent to:

$$I_{iso} = 2I_\parallel + 4I_\perp \sim I_v + I_h/2\,. \tag{15}$$

Our laser was vertically polarized, so we were measuring I_v. Q lines typically show the largest polarization effects because the active dipole moment is often perpendicular to the rotation axis of the molecule. Thus, we analyzed the fluorescence $I_\parallel$ and $I_\perp$ components with polarizers after pumping CH B–X(1,0) Q_1(8.5) (see Fig. 8). At laser powers close to those used for the absolute concentration measurements, there was partial polarization of the resulting fluorescence – the measured degree of polarization was $P \sim 0.25$, compared to a theoretical value $P = 0.5$. The fluorescence was not time-resolved and the effect of depolarizing collisions was integrated into the spectra. Rotational levels populated by relaxation retained some of the alignment. However, the alignment disappeared for the $B\ v' = 0$ populated by vibrational energy transfer. At high laser powers (Fig. 8), the partial polarization decreased to 0.2, but it did not vanish (as might be expected at complete saturation). Similar behavior has been shown by Rothe *et al.* [44] for OH A–X(3,0) excitation, and can be explained by collisional repopulation of the ground-state level by rotational relaxation. The ratio $I_\parallel/I_\perp$ for polarized fluorescence after pumping Q_1(8.5) is expected to be 1.33 [63]. Integrating the whole B–X(1,1) band, we found this ratio was approximately 1.15, consistent with partial polarization of the fluorescence.

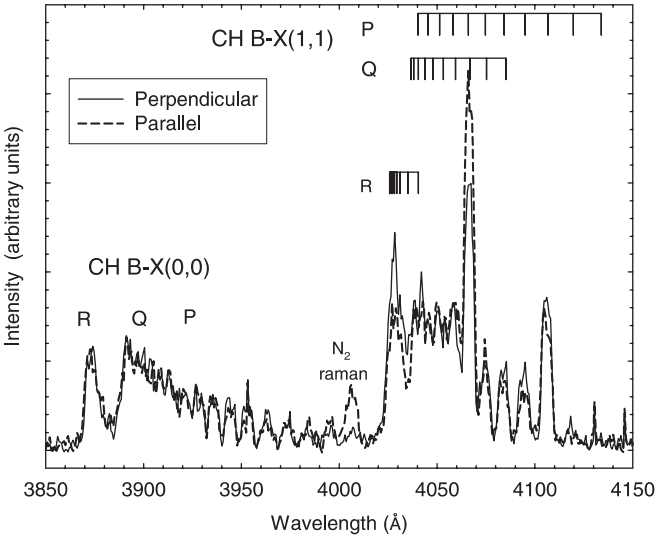

FIGURE 8 Polarization analysis of the dispersed fluorescence after CH B–X(1,0) Q_1(8) excitation in the premixed methane/air flame. Resolution is 5 Å (FWHM). Laser energy is 500 μJ/pulse or approximately 4×10^7 W cm^{-2}/cm^{-1} spectral irradiance

Following Doherty and Crosley [63], we pumped the Q_1(8.5) line with vertically polarized light and collected broadband fluorescence; this produced a small deviation from the isotropic excitation case with $I_v/I_{iso} = 1.05$. Pumping R_1(7.5), the ratio was $I_v/I_{iso} = 0.97$. These are maximum errors for totally polarized emission, and will be further reduced by partial collisional depolarization. The absence of polarization effects was confirmed by the statistically identical concentrations found with R_1(7.5) and Q_1(8.5) excitation.

An interesting case study of anisotropic polarization distributions with potential implications for absolute measurements is given by Nielsen *et al.* [64]. They found an experimental ratio $I_v/I_h = 3$, instead of the expected $I_v/I_h \sim 1$, exciting the OH A–X(2,0) band with a picosecond laser in an atmospheric-pressure flame. They attributed this difference to saturation of the molecular transition, leading to incomplete alignment. In the present experiment, we used nanosecond excitation pulses and were relatively far from saturation, so we did not expect such an effect in the I_v/I_h ratio. In any case, the maximum error expected from such an anisotropic fluorescence distribution is approximately 30% for excitation with vertical polarization. The Nielsen work also points out that not only the analysis of the perpendicular and parallel fluorescence components, but also the total fluorescence from different laser polarizations can be important in assessing the effects of polarization on the spatial distribution of the fluorescence.

We also note that polarization effects can be larger when the fluorescence is detected in isolated branches. Exciting an R line with vertically polarized light I_v and collecting the Q branch [67] can give a maximum of 20% extra fluorescence, while exciting with horizontally polarized light yields up to 40% less fluorescence. It is advisable not to use resolved branch detection in absolute LIF measurements to avoid unnecessary systematic errors.

4.2.6 Spatial resolution. The CH profile width from spectrograph-based measurements and from 2-D LIF images differ by a factor of two. The use of the spectrograph let us discriminate, in wavelength and space, the LIF and Raman signals simultaneously. Unfortunately, the spatial resolution obtained with our spectrograph was only approximately 500 μm, slightly larger than the width of the CH flame-front distribution. In the flame section where we carried out the calibration, the N_2 Raman signal distribution was about 2.5-mm wide (FWHM) and thus was not spatially degraded by the spectrograph. However, the CH flame front with an apparent width of 600 μm appeared much wider than it really was (see Fig. 6, plot in the right-hand side). To correct the number density determination performed with poor spatial resolution, we need to know the true width of the CH peak. From the flame 2-D LIF images, taken with a resolution of 150 μm, the CH profile was 300 μm. Gaussian deconvolution, to take into account the system resolution, brought the value to 250 μm (FWHM). This width agrees with our previous semiquantitative study in the same flame using pointwise LIF measurements [53]. Applying Gaussian deconvolution again to the spectrograph image (Fig. 6) gave a factor of 2.5 correction in the CH peak concentration. This problem arises from comparing signals with very different

spatial widths, one narrower than the instrumental spatial resolution. This correction will not be necessary with either better spatial resolution or with signals having the same width.

4.2.7 CH *number densities and spatial distribution.* Figure 9 shows the CH concentration image for the inner section of the premixed flame ($\Phi = 1.36$). This prompt NO intermediate and marker of the flame front was distributed in an almost perfect conical distribution. The figure shows a profile taken from the image at 12 mm above the burner exit plane. The profile is averaged only 0.16 mm (3 pixels) in height to avoid distortion due to the angular slant of CH in the cone. There is no interference from CH_2O LIF or CH chemiluminescence. The noise in the center region was produced primarily from the removal of the optical emission background. The CH peak is $(1.0 \pm 0.4) \times 10^{13}$ cm^{-3} or 2.4 ± 1 ppm at 1900 K. The peak concentration was constant within 20% for the whole flame front of the inner cone, consistent with observations by Herbele *et al.* [53].

The uncertainty in the CH concentration is considerable because of the many factors involved in the measurement and analysis. In our absolute CH determinations in low pressure flames, we estimated an average uncertainty of 25% and a maximum of 40% when implementing CH A–X(0,0) and B–X(0,0) excitation/detection schemes [1, 2]. These error bars have been shown to be realistic by recent CRD absorption experiments in a low pressure flame that agree to better than 20% [33]. At atmospheric pressure with the CH B–X(1,0) scheme, we estimate an uncertainty of 40%. The uncertainty in fluorescence quantum yield, lineshape integral and spectroscopic coefficients is slightly larger in the present approach. Spatial resolution problems and LIF modeling, although taken into account by the analysis, are an additional source of error in atmospheric pressure measurements. Improved spatial resolution and better knowledge of the collisional and radiative properties of the transition can reduce this error and make absolute LIF measurements at atmospheric pressure comparable in quality with low pressure determinations.

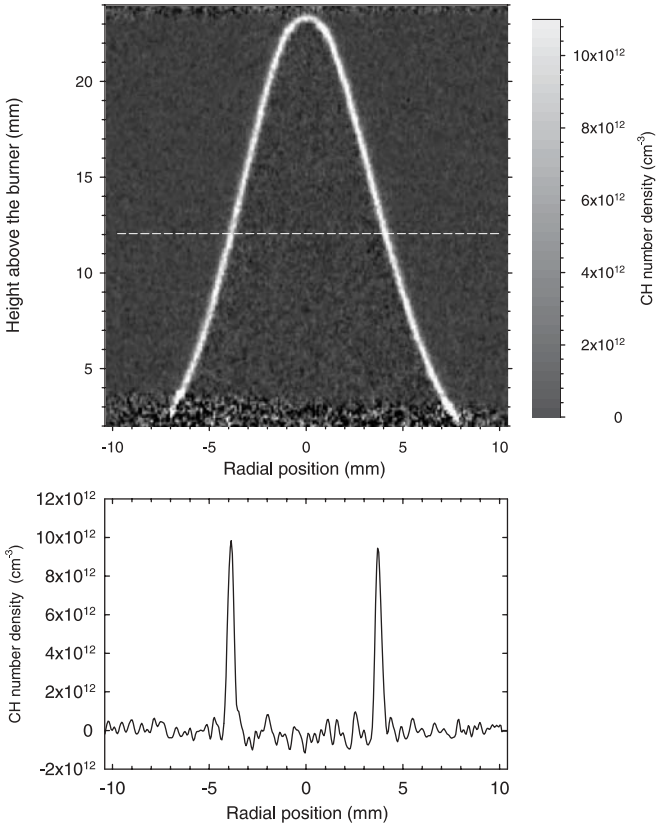

FIGURE 9 Absolute CH number density distribution by calibrated LIF image in the Bunsen flame's ($\Phi = 1.36$) partially premixed section. The *lower panel* contains a cross section taken 12 mm above the burner. The cross section was deconvoluted for spatial resolution effects and normalized to the measured absolute number density peak value

5 Conclusions

Absolute CH LIF measurements in atmospheric-pressure flames were obtained after assessing all the factors involved in the concentration determination. The LIF signal is linear with laser power even at levels high enough to deplete the pumped level of its initial population, because rotational relaxation repopulated the ground-state level during the nanosecond excitation pulse. Modeling of the laser excitation shows the LIF signal was proportional to the ground-state population, with a moderate dependence on various collisional relaxation processes involving ground- and excited-state levels. The collisions minimize the difference between the initial and steady-state populations of the rotational level during laser excitation. The remaining difference was the deviation from normal linear behavior. Modeling shows that this regime is apparently linear even at relatively high laser power, which we term "quasi-linear". Although the variation of the LIF signal with laser pulse energy was linear, the fraction of the ground-state population excited has to be determined. This quantitative signal assessment had to include rotational energy transfer considerations in both the ground- and excited-state manifolds. Corrections for spatial resolution limitations in the spectrograph were required to obtain accurate absolute CH concentrations. Polarization effects were found to be negligible in the current experimental scheme. The approach presented here for considering RET effects on the LIF power dependence can be applied to systems with no predissociative levels and to other chemical intermediates.

ACKNOWLEDGEMENTS This work was supported by the Basic Research Group of the Gas Research Institute and by the NASA Microgravity Combustion Research Program.

REFERENCES

1 J. Luque, D.R. Crosley: Appl. Phys. B **63**, 91 (1996)
2 J. Luque, G.P. Smith, D.R. Crosley: Proc. Combust. Inst. **26**, 959 (1996)
3 K.T. Walsh, M.B. Long, M.A. Tanoff, M.D. Smooke: Proc. Combust. Inst. **27**, 615 (1998)
4 W. Juchmann, H. Latzel, D.I. Shin, G. Peiter, T. Dreier, H.R. Volpp, J. Wolfrum, R.P. Lindstedt, K.M. Leung: Proc. Combust. Inst. **27**, 469 (1998)
5 I. Derzy, V.A. Lozovsky, S. Cheskis: Chem. Phys. Lett. **306**, 319 (1999)
6 I. Derzy, V.A. Lozovsky, S. Cheskis: Israel J. Chem. **39**, 49 (1999)
7 E.W. Diau, G.P. Smith, J.B. Jeffries, D.R. Crosley: Proc. Combust. Inst. **27**, 453 (1998)
8 P.A. Berg, G.P. Smith, J.B. Jeffries, D.R. Crosley: Proc. Combust. Inst. **27**, 1377 (1998)

9 D.R. Crosley, J.B. Jeffries, G.P. Smith: Israel J. Chem. **39**, 41 (1999)
10 L. Gasnot, P. Desgroux, J.F. Pauwels, L.R. Sochet: Combust. Flame **117**, 291 (1999)
11 X. Mercier, P. Jamette, J.F. Pauwels, P. Desgroux: Chem. Phys. Lett. **305**, 334 (1999)
12 X. Mercier, E. Therssen, J.F. Pauwels, P. Desgroux: Chem. Phys. Lett. **299**, 75 (1999)
13 J. Xie, B.A. Paldus, E.H. Wahl, J. Martin, T.G. Owano, C.H. Kruger, J.S. Harris, R.N. Zare: Chem. Phys. Lett. **284**, 387 (1998)
14 A. McIlroy: Chem. Phys. Lett. **296**, 151 (1998)
15 J.J. Scherer, D.J. Rakestraw: J. Chem. Phys. **265**, 169 (1997)
16 K.A. Peterson, D.B. Oh: Opt. Lett. **24**, 667 (1999)
17 M. Versluis, N. Georgiev, L. Martinsson, M. Alden, S. Kroll: Appl. Phys. B **65**, 411 (1997)
18 A.C. Eckbreth: *Laser Diagnostics for Combustion Temperature and Species*, 2nd edn. (Gordon and Breach, Amsterdam 1996)
19 J.J. Scherer, J.B. Paul, A. O'Keefe, R.J. Saykally: Chem. Rev. **97**, 25 (1997)
20 A. McIlroy, J.B. Jeffries: In: *Applied Combustion Diagnostics*, ed. by K. Kohse-Hoeinghaus, J.B. Jeffries (Taylor and Francis, New York 2002) p. 98
21 L. Lynds, B.A. Woody: Appl. Opt. **27**, 1225 (1988)
22 D.E. Heard, J.B. Jeffries, G.P. Smith, D.R. Crosley: Combust. Flame **88**, 137 (1992)
23 D.I. Shin, T. Dreier, J. Wolfrum: Appl. Phys. B **72**, 257 (2001)
24 C. Cunge, J.P. Booth, J. Derouard: Chem. Phys. Lett. **263**, 645 (1996)
25 M. Engelhard, W. Jacob, W. Moller, A.W. Koch: Appl. Opt. **34**, 4542 (1995)
26 P.A. Bonczyk, J.A. Shirley: Combust. Flame **34**, 253 (1979)
27 C. Kaminski, P. Ewart: Appl. Phys. B **61**, 585 (1995)
28 J.A. Vanderhoff, R.A. Beyer, A.J. Kotlar, W.R. Anderson: Combust. Flame **49**, 197 (1983)
29 J. Luque, W. Juchmann, J.B. Jeffries: J. Appl. Phys. **82**, 2072 (1997)
30 J.T. Salmon, N.M. Laurendeau: Appl. Opt. **24**, 65 (1985)
31 W.K. Bischel, D.J. Bamford, L.E. Jusinski: Appl. Opt. **25**, 1215 (1986)
32 J. Luque, J.B. Jeffries, G.P. Smith, D.R. Crosley: Appl. Phys. B **73**, 731 (2001)
33 J. Luque, J.B. Jeffries, G.P. Smith, D.R. Crosley, J.J. Scherer: Combust. Flame **126**, 1725 (2001)
34 A.P. Baronavski, J R. McDonald: Appl. Opt. **16**, 1897 (1977)
35 K. Kohse-Hoinghaus, W. Perc, T. Just: Ber. Bunsenges. Phys. Chem. **87**, 1052 (1983)
36 K. Kohse-Hoinghaus, R. Heidenreich, T. Just: Proc. Combust. Inst. **20**, 1177 (1984)
37 J. Luque, W. Juchmann, J.B. Jeffries: Appl. Opt. **36**, 3261 (1997)
38 R.G. Joklik, J.W. Daily, W.J. Pitz: Proc. Combust. Inst. **21**, 895 (1986)
39 J.W. Thoman, A. McIlroy: J. Phys. Chem. A **104**, 4953 (2000)
40 R. Evertsen, R.L. Stolk, J.J. ter Meulen: Combust. Sci. Technol. **149**, 19 (1999)
41 J. Luque, R.J.H. Klein-Douwel, J.B. Jeffries, D.R. Crosley: Appl. Phys. B **71**, 85 (2000)
42 N. Elander, M. Hehenberger, P.R. Bunker: Phys. Scripta **20**, 631 (1979)
43 J. Luque, J.B. Jeffries, G.P. Smith, D.R. Crosley: Chem. Phys. Lett. **346**, 209 (2001)
44 E.W. Rothe, Y.W. Gu, G.P. Reck: Appl. Opt. **35**, 934 (1996)
45 E.W. Rothe, Y. Gu, A. Chryssostomou, P. Andresen, F. Bormann: Appl. Phys. B **66**, 251 (1998)
46 W.P. Partridge, N.M. Laurendeau: Appl. Opt. **34**, 2645 (1995)
47 J.W. Daily, E.W. Rothe: Appl. Phys. B **68**, 131 (1999)
48 F. Bormann, T. Nielsen, M. Burrows, P. Andresen: Appl. Phys. B **62**, 601 (1995)
49 M. Kind, F. Stuhl: J. Chem. Phys. **114**, 6160 (2001)
50 C. Nokes, G. Gilbert, R.J. Donovan: Chem. Phys. Lett. **99**, 491 (1983)
51 R.J.H. Klein-Douwel, J. Luque, J.B. Jeffries, G.P. Smith, D.R. Crosley: Appl. Opt. **39**, 3712 (2000)
52 R.J.H. Klein-Douwel, J. Luque, J.B. Jeffries, G.P. Smith, D.R. Crosley: Appl. Opt. **41**, 1174 (2002)
53 N. Heberle, G.P. Smith, J.B. Jeffries, D.R. Crosley, R.W. Dibble: Appl. Phys. B **71**, 733 (2000)
54 A.J. Dean, R.K. Hanson: J. Quant. Spectrosc. Radiat. Transfer **42**, 375 (1989)
55 Y. Takubo, H. Yano, H. Matsuoka, M. Shimazu: J. Quant. Spectrosc. Radiat. Transfer **30**, 163 (1983)
56 D.A.V. Kliner, R.L. Farrow: J. Chem. Phys. **110**, 412 (1999)
57 J. Luque, D.R. Crosley: Appl. Opt. **99**, 1423 (1999)
58 J. Luque, D.R. Crosley: LIFBASE v1.61 (SRI International, MP-99-0099, (www.sri.com/cem/lifbase) 1999)
59 J. Luque, D.R. Crosley: J. Chem. Phys. **104**, 3907 (1996)
60 J. Brzozowski, P. Bunker, N. Elander, P. Erman: Astrophys. J. **207**, 414 (1976)
61 C.C. Wang, L. Nemes, K.C. Lin: Chem. Phys. Lett. **245**, 585 (1995)
62 J. Luque, D.R. Crosley: J. Chem. Phys. **102**, 439 (1998)
63 P.M. Doherty, D.R. Crosley: Appl. Opt. **23**, 713 (1984)
64 T. Nielsen, F. Bormann, M. Burrows, P. Andresen: Appl. Opt. **30**, 7960 (1997)
65 A. Brockhinke, W. Kreutner, U. Rahmann, K. Kohse-Hoinghaus, T.B. Settersen, M.A. Linne: Appl. Phys. B **69**, 477 (1999)
66 P. Beaud, P.P. Radi, D. Franzke, H.M. Frey, B. Mischler, A.P. Tzannis, T. Gerber: Appl. Opt. **37**, 3354 (1998)
67 Y.C. Chen, M.S. Mansour: Appl. Phys. B **64**, 599 (1997)